

**Effects of Precipitation on Ocean Mixed-Layer Temperature and Salinity
as Simulated in a 2-D Coupled Ocean-Cloud Resolving Atmosphere Model**

Xiaofan Li^{1,2}, C.-H. Sui, K.-M. Lau, D. Adamec
NASA/Goddard Space Flight Center, Greenbelt, Maryland

Submitted to *J. Meteor. Soc. Japan*

September, 1999

¹Current affiliation: SM & A Corporation, Arlington, Virginia

²Corresponding author address: Dr. X. Li, SM & A, NASA/GSFC, Code 913, Greenbelt,
MD 20771. < *email* > xli@climate.gsfc.nasa.gov

Abstract

A two-dimensional coupled ocean-cloud resolving atmosphere model is used to investigate possible roles of convective scale ocean disturbances induced by atmospheric precipitation on ocean mixed-layer heat and salt budgets. The model couples a cloud resolving model with an embedded mixed layer-ocean circulation model. Five experiments are performed under imposed large-scale atmospheric forcing in terms of vertical velocity derived from the TOGA COARE observations during a selected seven-day period. The dominant variability of mixed-layer temperature and salinity are simulated by the coupled model with imposed large-scale forcing.

The mixed-layer temperatures in the coupled experiments with 1-D and 2-D ocean models show similar variations when salinity effects are not included. When salinity effects are included, however, differences in the domain-mean mixed-layer salinity and temperature between coupled experiments with 1-D and 2-D ocean models could be as large as 0.3 PSU and $0.4^{\circ}C$ respectively. Without fresh water effects, the nocturnal heat loss over ocean surface causes deep mixed layers and weak cooling rates so that the nocturnal mixed-layer temperatures tend to be horizontally-uniform. The fresh water flux, however, causes shallow mixed layers over convective areas while the nocturnal heat loss causes deep mixed layer over convection-free areas so that the mixed-layer temperatures have large horizontal fluctuations. Furthermore, fresh water flux exhibits larger spatial fluctuations than surface heat flux because heavy rainfall occurs over convective areas embedded in broad non-convective or clear areas, whereas diurnal signals over whole model areas yield high spatial correlation of surface heat flux. As a result, mixed-layer salinities contribute more to the density differences than do mixed-layer temperatures.

1. Introduction

Precipitation and associated salinity stratification affect the sea surface temperature (SST) through changing mixed-layer depth (e.g., Miller et al. 1976; Li et al. 1998), and upper ocean thermal structure through forming a barrier layer between the halocline and the thermocline (e.g., Godfrey and Linstrom 1989; Lukas and Linstrom 1991; You 1995; Vialard and Delecluse 1998a,b). Miller (1976) found precipitation could induce shallower mixed-layers in numerical simulations. Since the effect of heating/cooling is inversely related to the depth of the mixed layer, shallower mixed layers will undergo larger temperature changes than deeper mixed layers with the same thermal forcing. Li et al. (1998) found that salinity stratification can cause instances when entrainment will result in warming the mixed layer as opposed to the normal cooling associated with entrainment. Cooper (1988) demonstrated the importance of salinity in numerical simulations of the Indian Ocean and found that salinity effects could account for as much as a 0.5°C temperature bias and a 0.1 m s^{-1} velocity bias near the surface after 110 days of integration. In their ocean modeling study, Murtugudde and Busalacchi (1998) found that the differences of annual mean SST between the simulations with salinity and climatological precipitation and without cloud be as much as 0.5°C , indicating the inclusion of salinity effects is necessary to simulate realistic climatic systems. Yang et al. (1998) also found that in the western Pacific warm pool SST would be 0.6°C lower if there were no salinity effect associated with precipitation. Delcroix et al. (1998) analyzed sea surface salinity (SSS) along a shipping track running from Fuji to Japan and found that drastic changes of SSS in the warm and fresh pool region during the 1996 La Nina and the 1997 El Nino are associated with the changes of precipitation, equatorial upwelling and downwelling, and equatorial current, suggesting the potential impacts of precipitation and salinity stratification in simulation of El Nino-Southern Oscillation. Sui et al. (1997b) found a sensitivity of the mixed-layer temperature to temporal scale of the atmospheric forcing in the simulations of the mixed-layer model during Tropical Ocean Global Atmosphere (TOGA)-Coupled Ocean Atmosphere Response Experiment (COARE) Intensive Observation Period (IOP).

Due to limitation of computation resource, the time step and horizontal grid lengths of

the ocean general circulation model (OGCM) are usually much larger than the temporal and spatial scales of the atmospheric convections. Thus, the effects of convective scale ocean disturbances induced by atmospheric convection through surface heat and fresh water fluxes on ocean mixed-layer heat and salt budgets should be evaluated. A coupled ocean-cloud resolving atmosphere model developed at Goddard Space Flight Center is a unique tool for such evaluation. The objective of this study is to analyze the differences in ocean mixed-layer between the experiments with 1-D ocean model forced by horizontally-mean atmospheric surface fluxes and with 2-D ocean model forced by spatially-dependent atmospheric surface fluxes, and the physical processes responsible for these differences.

The description of the coupled model and the experiment designs are given in section 2. In section 3, the differences in the ocean mixed layers between 1-D and 2-D ocean simulations with and without salinity effects are first analyzed to show the important impacts of precipitation-induced convective scale ocean disturbances on horizontal-mean mixed-layer variations. The horizontal distributions and time evolutions of the disturbances, and the physical processes by which the disturbances affect horizontal-mean mixed-layer thermal and salt budgets are then discussed. The findings are summarized in section 4.

2. Coupled ocean-cloud resolving atmosphere model and experiment designs

The coupled model consists of two components: a cloud resolving atmosphere model, and an embedded mixed layer-ocean circulation model. The cloud resolving model was originally developed by Soong and Ogura (1980), Soong and Tao (1980), and Tao and Simpson (1993). The governing equations with an anelastic approximation can be expressed as follows:

$$\frac{\partial u'}{\partial x} + \frac{1}{\bar{\rho}} \frac{\partial}{\partial z} \bar{\rho} w' = 0, \quad (1)$$

$$\begin{aligned} \frac{\partial A'}{\partial t} = & -\frac{\partial}{\partial x} (u' \bar{A}^o + \bar{u}^o A') - \frac{1}{\bar{\rho}} \frac{\partial}{\partial z} \bar{\rho} (w' \bar{A}^o + \bar{w}^o A') - \frac{\partial}{\partial x} (u' A' + \overline{u' A'}) \\ & - \frac{1}{\bar{\rho}} \frac{\partial}{\partial z} \bar{\rho} (w' A' - \overline{w' A'}) + S_A - \bar{S}_A + D_A - \bar{D}_A, \end{aligned} \quad (2)$$

$$\begin{aligned} \frac{\partial B}{\partial t} = & -\frac{\partial(u'B')}{\partial x} - \bar{u}^o \frac{\partial B'}{\partial x} - \frac{1}{\bar{\rho}} \frac{\partial}{\partial z} \bar{\rho} w' B' - \bar{w}^o \frac{\partial B'}{\partial z} - w' \frac{\partial \bar{B}}{\partial z} \\ & + S_B + D_B - \bar{u}^o \frac{\partial \bar{B}^o}{\partial x} - \bar{w}^o \frac{\partial \bar{B}}{\partial z}, \end{aligned} \quad (3)$$

$$\frac{\partial C}{\partial t} = -\frac{\partial(uC)}{\partial x} - \frac{1}{\bar{\rho}} \frac{\partial}{\partial z} \bar{\rho}(w - w_{TV})C + S_C + D_C. \quad (4)$$

Here $A = (u, w)$, u , and w are zonal, and vertical air wind components; $B = (\theta, q_v)$, θ and q_v are air potential temperature and specific humidity respectively; $C = (q_c, q_r, q_i, q_s, q_g)$, q_c, q_r, q_i, q_s , and q_g are the mixing ratios of cloud water, rain, cloud ice, snow, and graupel, respectively; $\bar{\rho}$ is a mean air density which is a function of height only; w_{TV} is a terminal velocity which is zero for cloud water and ice; S_A is a source and sink in momentum equations, such as pressure gradient force, buoyancy force; S_B is a source and sink in potential temperature and moisture equations, such as latent heat due to condensation, and radiative heating and cooling; S_C is source and sink of cloud content determined by microphysical processes (Li et al. 1999); D_A, D_B , and D_C are dissipation terms.

In the derivations of equations (1)-(3), Reynold's area average is applied to A and B $A = \bar{A} + A'$, and $B = \bar{B} + B'$, where \bar{A}, \bar{B} and A', B' denote area means and deviations of A and B , respectively. Regarding the area mean quantities in the above equations as the observed large-scale variables, Soong and Ogura (1980) first developed ways to impose the observed large-scale variables in a cloud resolving model to examine the "one-way" response of the model to the imposed "large-scale forcing". In this study, observed \bar{u}^o and \bar{w}^o are imposed in the model so only perturbation momentums are predicted by using (2) for the momentum simulations where the area mean variables \bar{u} and \bar{w} are replaced by \bar{u}^o and \bar{w}^o . Hereafter, superscript o denotes imposed observed variables in the model. As first suggested by Soong and Ogura (1980), the cloud resolving model here is imposed by zonally uniform vertical velocity (\bar{w}^o) and zonal wind (\bar{u}^o) as well as horizontal advection ($-\bar{u}^o \frac{\partial \bar{B}^o}{\partial x}$). The assumption that $u' \frac{\partial \bar{B}^o}{\partial x} = 0$ is also used in the derivation of (3). The detailed derivations can be referred to Li et al. (1999).

The radiation parameterization schemes used in the model were developed by Chou et al. (1997) for solar radiation and by Chou et al. (1991) and Chou and Suarez (1994) for infrared radiation. The cloud microphysics parameterization schemes developed by Krueger et al. (1995) along with other microphysics schemes are also used in the model. A detailed description of a 2-D version of the model used in the current study can be found in Sui et al. (1998a) and Li et al. (1999).

The embedded mixed layer-ocean circulation model used in this study was originally developed by Adamec et al. (1981). The mixed-layer equations are

$$\frac{\partial h_m}{\partial t} + \frac{\partial u_m h_m}{\partial x} = W_e, \quad (5a)$$

$$\frac{\partial u_m}{\partial t} = -\frac{W_e}{h_m} \mathcal{H}(W_e)(u_m - u_e) - \frac{\tau_o}{\rho_r h_o}, \quad (5b)$$

$$\frac{\partial T_m}{\partial t} = -\frac{W_e}{h_m} \mathcal{H}(W_e)(T_m - T_e) + \frac{Q_o + I(0) - I(h_m)}{\rho_r c_w h_m}, \quad (5c)$$

$$\frac{\partial S_m}{\partial t} = -\frac{W_e}{h_m} \mathcal{H}(W_e)(S_m - S_e) - \frac{S_m(P - E)}{\rho_r h_m}, \quad (5d)$$

where u_m , h_m , T_m , and S_m are ocean mixed-layer current, depth, temperature, and salinity, respectively; u_e , T_e and S_e , are the ocean current, temperature, and salinity of the level just beneath the mixed layer, respectively; c_w is heat capacity of water; ρ_r denotes a constant reference seawater density; \mathcal{H} is the Heavyside step function; τ_0 is the surface wind stress; h_o is the depth of the Ekman layer; $I = I_o[r e^{-\gamma_1 z} + (1-r)e^{-\gamma_2 z}]$, and I_o is solar radiation at the ocean surface, and γ_1 , γ_2 are attenuation parameters for solar radiation penetration, and z is positive downward with $z = 0$ being the ocean surface; Q_o is a flux at the ocean surface, which includes long wave radiation, sensible and latent heat; P and E denote rates of precipitation and evaporation at the ocean surface, respectively; W_e is the entrainment velocity at the mixed-layer base, which can be obtained by calculating Kraus-Turner's equation which was originally derived by Niiler and Kraus (1977) and modified in Sui et al. (1997b) and is similar to Gaspar (1988),

$$\begin{aligned} & W_e \mathcal{H}(W_e) h_m g [\alpha(T_m - T_e) - \beta(S_m - S_e)] \\ & = 2m_s u_*^3 - \frac{h_m}{2} [(1 + m_b) B_o + (1 - m_b) |B_o|], \end{aligned} \quad (6)$$

$$B_o = \frac{g\alpha}{\rho_r c_w} < Q_o + [1 + r e^{-\gamma_1 h_m} + (1-r)e^{-\gamma_2 h_m} - \frac{2r}{\gamma_1 h_m}(1 - e^{-\gamma_1 h_m}) - \frac{2(1-r)}{\gamma_2 h_m}(1 - e^{-\gamma_2 h_m})] I_o > + \frac{g}{\rho_r} \beta S_m (P - E), \quad (6a)$$

where u_* is surface friction velocity; α and β describe the logarithmic expansion of ocean water density ρ as functions of temperature and salinity, respectively; g is gravitational acceleration; m_s and m_b are turbulent mixing factors due to wind stirring and convection, respectively.

The two-dimensional model equations on the equator are,

$$\frac{\partial u_1}{\partial t} = -\frac{\partial u_1 u_1}{\partial x} - \frac{\partial w_1 u_1}{\partial z} + A_M \frac{\partial^2 u_1}{\partial x^2} + K_M \frac{\partial^2 u_1}{\partial z^2}, \quad (7a)$$

$$\frac{\partial T}{\partial t} = -\frac{\partial u_1 T}{\partial x} - \frac{\partial w_1 T}{\partial z} + A_T \frac{\partial^2 T}{\partial x^2} + K_T \frac{\partial^2 T}{\partial z^2} - \frac{1}{\rho_r c_w} \frac{\partial I}{\partial z}, \quad (7b)$$

$$\frac{\partial S}{\partial t} = -\frac{\partial u_1 S}{\partial x} - \frac{\partial w_1 S}{\partial z} + A_S \frac{\partial^2 S}{\partial x^2} + K_S \frac{\partial^2 S}{\partial z^2}, \quad (7c)$$

$$\frac{\partial u_1}{\partial x} + \frac{\partial w_1}{\partial z} = 0, \quad (7d)$$

$$\frac{\partial p}{\partial z} = -\rho g, \quad (7e)$$

$$\rho = \rho_r [1 - \alpha(T - T_r) + \beta(S - S_r)], \quad (7f)$$

where u_1 and w_1 are zonal and vertical components of ocean circulation, respectively; A_M , A_T and A_S are horizontal momentum, heat and salinity diffusivity coefficients, respectively; K_M , K_T and K_S are vertical momentum, heat and salinity diffusivity coefficients, respectively; T_r and S_r are the reference temperature and salinity, respectively; The mixed-layer model and the circulation model communicate with each other through the embedding technique described by Adamec et al. (1981). The model also includes a convective adjustment scheme which ensures the static stability of the upper ocean.

The cloud model that is imposed by a horizontally uniform forcing requires a cyclic lateral boundary condition. Thus, the cyclic lateral boundary condition is used in both the cloud and ocean models. The cyclic lateral boundary does not allow meridional variations of Earth vorticity. Thus, the coupled model is only applied to an x-z frame along the

equator in this study. Such a model excludes the upwelling and downwelling associated with the Ekman transport. However, considering the life span of individual convective cloud that produces significant amount of precipitation into ocean at about 1-2 hour, the corresponding frequency ($1.4 - 2.8 \times 10^{-4} \text{ s}^{-1}$) is much larger than the Coriolis frequency ($0.7 \times 10^{-4} \text{ s}^{-1}$) within $30^\circ S - 30^\circ N$. Therefore, the upwelling is not considered in this study.

The horizontal model domain is 768 km, and a horizontal grid resolution is 1.5 km in the coupled model. The vertical grid resolution ranges from about 200 m near the surface to about 1 km around 100 mb in the cloud model, and from about 1 meter in the upper levels to about 50 meters in the lower levels in the ocean model. The depth of the ocean model is 500 meters. A time step of 12 seconds is used in both the cloud and ocean mixed-layer models. The initial air temperature and specific humidity and initial ocean temperature and salinity are zonally uniform. The vertical profiles of air temperature and specific humidity are taken from the TOGA COARE observations (Sui et al. 1997a), and the vertical profiles of ocean temperature and salinity are constructed from observations from the IMET buoy, and the TOGA TAO mooring (McPhaden 1993; 1995) at $156^\circ E$, $2^\circ S$ during the TOGA COARE IOP. The vertical distribution of solar radiation is defined by setting $r = 0.77$, $\gamma_1^{-1} = 0.65m$, and $\gamma_2^{-1} = 14m$ (Sui et al. 1998b). The other parameters for the ocean model used in this study are: $m_s = 0.4$, $m_b = 0.2$, $\alpha = 2 \times 10^{-4} \text{ }^\circ C^{-1}$, $\beta = 7.5 \times 10^{-4} \text{ PSU}^{-1}$, $\rho_r = 1027.6 \text{ kgm}^{-3}$, $c_w = 4218 \text{ J}^\circ C^{-1} \text{ kg}^{-1}$, $T_r = 10^\circ C$, $S_r = 35 \text{ PSU}$, $h_o = 11 \text{ m}$, $A_M = A_T = A_S = 200 \text{ m}^2 \text{ s}^{-1}$, $K_M = 10^{-4} \text{ m}^2 \text{ s}^{-1}$, $K_T = K_S = 10^{-5} \text{ m}^2 \text{ s}^{-1}$.

Five experiments are carried out in this study (Table 1). In all experiment, the model is integrated for seven days with the same imposed varying horizontally-uniform observed atmospheric forcings (vertical velocity, zonal wind, and horizontal temperature and moisture advectations) and the same initial horizontally-uniform conditions. The observed atmospheric forcings are taken from a particular TOGA COARE period (4 a.m. 18 - 4 a.m. 25 December 1992). Only the last six days of the simulation for each experiment are analyzed. C1 uses the cloud model only in which horizontally-uniform SST is imposed

by hourly observed data at the IMET buoy (Li et al. 1999). In CA, the embedded mixed layer-ocean circulation model is degraded to a 1-D mixed-layer model. The mixed-layer model is forced by the horizontal-mean fluxes at each time step. The experiment setup in CB is identical to that in CA except that CB uses a 2-D ocean model (forced with spatially dependent fluxes). CA and CB test the effects of atmospheric convection on the ocean mixed-layer directly through fresh water flux and salinity stratification. CAT and CBT are the same as CA and CB, respectively, except that salinity effects are excluded in the ocean model. CAT and CBT test the effects of atmospheric convection on the ocean mixed-layer indirectly through surface heat fluxes (especially solar radiative flux) in the absence of fresh water flux and salinity.

3. Results

Fig. 1 shows the time evolution of vertical distribution of the large-scale atmospheric vertical velocity and zonal wind during 19-25 December 1992 that are imposed in the model. Strong upward motions with maxima of $15 - 25 \text{ mb hour}^{-1}$ occur on late 20 December, and during the early mornings of 23 and 25 December between 400 and 500 mb. The latter two maxima are quasi-two-day oscillations (Takayabu et al. 1996) in the convective phase of an intraseasonal oscillation during COARE. Two less intense upward motion centers appear during the nights of 19 and 21 December. The occurrence of maximum upward motion each night is consistent with the diurnal signals observed by Sui et al. (1997a). The large scale zonal wind in the lower troposphere (below 700 mb) are westerly that strengthens to 10 m s^{-1} around 23 December. The mid-troposphere has an easterly-westerly wind oscillation with maximum easterly wind of -10 m s^{-1} at 500 mb on 20 December. The upper troposphere (above 250 mb) is dominated by easterly winds. As mentioned previously, the model is also forced by the observed horizontal temperature and moisture advectons (not shown), which have smaller amplitudes than the vertical advectons respectively.

The time evolution of the horizontal-mean surface wind stress, net surface heat flux, and surface fresh water flux simulated by the coupled model in the four experiments is similar to that simulated by the cloud resolving model with imposed observed SST in

C1. As an example, Fig. 2 is the time evolution of the surface fluxes in C1 (solid) and CA (dashed). They display remarkable similarities in both phase and amplitude. The maximum differences of the time-means of surface wind stress, net surface heat flux, and surface fresh water flux among the five experiments are about $0.002 Nm^{-2}$, $7.9 Wm^{-2}$, and $1.1 \times 10^{-5} kgm^{-2}s^{-1}$, respectively (Table 2). These coupled experiments generate similar zonal-mean results in the atmosphere (not shown), which is attributed to the strong control by same imposed vertical velocity. The coupled model also simulates mixed-layer properties reasonably well (e.g., Fig. 3). The RMS differences of mixed-layer temperature and 3-m salinity between the simulation in CA (1-D model) and the observation at IMET buoy are $0.28^{\circ}C$ and $0.09 PSU$, respectively.

3a. Differences in the mixed-layer variations between 1-D and 2-D ocean simulations

The differences in the mixed-layer thermal and saline variations between 1-D and 2-D ocean simulations with salinity effects are first analyzed. Fig. 4 shows that the mixed-layer temperature and salinity in CA (light dashed) and the horizontal-mean mixed-layer temperature and salinity in CB (dark solid). The mixed-layer temperatures in both CA and CB are about the same on 19-20 December (Fig. 4). From the late evening of 20 to the early morning of 22 December, the temperature in CA becomes lower than that in CB. After noon 22 December, the temperature in CA becomes higher than that in CB. The temperature variations can be explained by the mean thermal budget in the mixed layer that consists of the thermal entrainment, surface thermal forcing, and thermal advection. In CB, surface thermal forcing determines the temperature variations in the mixed layer, with modifications from warm water entrainment during nighttime (Fig. 5a). Thermal advection is small compared to surface thermal forcing and thermal entrainment. The mean thermal budget around midnight of 20 and early morning of 21 December listed in Table 3a shows that the surface thermal forcings are dominant in heat budgets in both cases. The net cooling rate in CA ($-2.07^{\circ}Cday^{-1}$) is more than twice as large as in CB ($-0.89^{\circ}Cday^{-1}$), which causes a larger temperature drop in CA during this period. The heat budget over the period of the afternoon and evening of 22 December is shown in Table 3b. In CA, the mean thermal entrainment ($0.61^{\circ}Cday^{-1}$) offsets the mean surface thermal

forcing ($-0.54^{\circ}C day^{-1}$) so that the temperature change is small. In CB, the mean cooling due to surface thermal forcing ($-0.92^{\circ}C day^{-1}$) overcomes the heating by mean thermal entrainment ($0.38^{\circ}C day^{-1}$) so that the temperature drops.

The horizontal-mean mixed-layer salinity in CA and CB (Fig. 4b) shows that they are similar for the first three days. After 22 December, the salinity in CB becomes 0.3 *PSU* lower than that in CA. The salinity variations can be also examined in terms of the mean salt budget in the mixed layer, including the saline entrainment, fresh water forcing, and salinity advection. In CB, fresh water forcing determines salinity variations in the mixed layer, with modification from salty water entrainment, and salinity advection is small during rainfall (Fig. 5b). During clear sky, salinity advection, saline entrainment and forcing are equally important. The budget on the morning of 22 December (Table 4) shows that in CB, the mean saline entrainment ($0.17 \text{ PSU day}^{-1}$) and advection ($0.16 \text{ PSU day}^{-1}$) are offset by mean fresh water forcing ($-0.34 \text{ PSU day}^{-1}$) so that the salinity remains near 33.9 *PSU*, whereas in CA the magnitude of mean saline entrainment ($0.33 \text{ PSU day}^{-1}$) is twice as large as that of mean fresh water forcing ($-0.16 \text{ PSU day}^{-1}$) so that the mixed-layer salinity increases to 34.2 *PSU*.

The experiments without salinity effects (CAT and CBT) are carried out and then compared with the experiments with salinity effects (CA and CB) to highlight the effects of precipitation on mixed-layer thermal and salt variations. The horizontal-mean mixed-layer temperatures are higher in CAT and CBT than those in CA and CB (in particular within 20-23 December) (Fig. 4). This is attributed to the much deeper mixed layers in CAT and CBT that lead to smaller cooling rates (see Table 3a). The temperature differences between CAT and CBT are near zero during nighttime and reach maximum ($0.15^{\circ}C$) during daytime. The maximum temperature difference between CAT and CBT is smaller than that between CA and CB ($0.4^{\circ}C$). The thermal variations are similar in CAT and CBT whereas they are different between CA and CB.

To further analyze causes of differences in horizontal-mean mixed-layer variations between 1-D and 2-D ocean simulations, some quantities related to surface fluxes and mixed-

layer properties are analyzed, which are defined by

$$TF = \frac{Q_o + I(0) - I(h_m)}{\rho_r c_w}, \quad (8a)$$

$$SF = -\frac{S_m(P - E)}{\rho_r}, \quad (8b)$$

$$STF = \left\langle \frac{TF}{h_m} \right\rangle, FWF = \left\langle \frac{SF}{h_m} \right\rangle, \quad (8c)$$

$$STF1 = \frac{\langle TF \rangle}{\langle h_m \rangle}, FWF1 = \frac{\langle SF \rangle}{\langle h_m \rangle}. \quad (8d)$$

Here, TF and SF are proportional to surface heat flux and fresh water flux, respectively. The angle bracket ($\langle \rangle$) is the horizontal mean.

Since the cloud model is imposed by the same forcing, the horizontal-mean surface heat fluxes, and fresh water fluxes as well as the wind stresses (not shown) are very similar in CAT and CBT (Fig. 6a), and in CA and CB (Figs. 6b, 6c). When the mixed-layer depth that is less (more) than 30 m, the horizontal-mean mixed layers are deeper (shallower) in CBT than in CAT (Fig. 6d). The horizontal-mean mixed layers are deeper in CB than in CA (Fig. 6e). The differences of the horizontal-mean mixed-layer depths between CAT and CBT and between CA and CB show that the surface fluxes determine the mixed-layer depth in nonlinear ways, and suggest the important impacts of convective scale ocean disturbances induced by atmospheric precipitation on horizontal-mean mixed-layer depths.

The different horizontal-mean mixed-layer depths further cause different horizontal-mean surface thermal and fresh water forcings (Fig. 7). Fig. 7a show two basic modes in CBT. Similarity mode that is along the diagonal line denotes similarity between STF and STF1. Difference mode that is away from the diagonal line measures difference between STF and STF1 in which the magnitude of STF is larger than that of STF1. Difference mode predicts the potential difference in thermal variations between 1-D and 2-D ocean simulations. Fig. 7b displays weak difference mode which is more oriented to similarity mode. A weak difference mode guarantees similar thermal variabilities in CAT and CBT. The stronger STF values in CAT (Fig. 7b) than the corresponding STF1 values in CBT (Fig. 7a) indicate the effect of shallower mixed layers in CAT. The stronger difference

mode appears in STF of CB versus CA (Fig. 7d), in which the magnitude of STF is much stronger in CA than in CB. This difference mode cause large thermal variations in CA compared to CB. The difference mode of STF in CA and CB differs significantly from that expected by STF1 in CB (Fig. 7c). Difference mode of FWF versus FWF1 predicted in CB only explains a part of difference mode of FWF simulated in CA and CB (Figs. 7e, and 7f), in which FWF in CB is larger than that in CA as well as FWF1 in CB. The difference modes in STF versus STF1 and in FWF versus FWF1 simulated by 2-D ocean model, and difference modes in 1-D and 2-D ocean simulations show important nonlinear effects of convective scale ocean disturbances on surface thermal and fresh water forcings. These will be analyzed in the next subsection.

3b. The role of convective scale disturbances in the mixed layer

Before the effects of convective scale ocean disturbances are examined, time evolution of horizontal distributions of surface precipitation, mixed-layer temperature, salinity, and depth simulated in CB are shown in Fig. 8. Although the diurnal signals of mixed-layer temperature and depth associated with the diurnal solar radiation can be clearly seen, the fresh water flux associated with the surface precipitation causes highly non-uniform horizontal distributions of the mixed-layer properties (Fig. 8). One way to examine the effects of convective scale ocean disturbances is to calculate horizontal-mean and anomaly budgets directly by separating the quantities into horizontal mean and anomaly. Unfortunately, it is difficult to do so because the entrainment and forcing are inversely proportional to the mixed-layer depth, and the depth anomalies (Fig. 10c) from the horizontal-mean depths (Fig. 4c) have the same orders of magnitudes as the horizontal-mean depths have.

An alternative to estimate the contributions of convective scale disturbances to the horizontal-mean (large-scale) temperature and salinity in CB is to analyze the linear correlation coefficients (R_i) and the RMS differences (D_j) between the horizontal-mean value and grid values of the mixed-layer properties. R_i and D_j of any variable (F) in the ocean mixed layer are defined by

$$R_i = \left[\sum_{j=1}^N (\langle F \rangle_j - \langle \bar{F} \rangle) (F_{i,j} - \bar{F}_i) \right]$$

$$/[\sum_{j=1}^N (\langle F \rangle_j - \langle \bar{F} \rangle)^2 \sum_{j=1}^N (F_{i,j} - \bar{F}_i)^2]^{\frac{1}{2}}, \quad (9a)$$

$$D_j = [\frac{1}{M} \sum_{i=1}^M (F_{i,j} - \langle F \rangle_j)^2]^{\frac{1}{2}}, \quad (9b)$$

where subscripts i and j are the discrete numbers for zonal and time indices; $N=144$ is the total discrete number for j ; $M=512$ is the total discrete number for i ; The overbar ($\bar{\quad}$) denotes time mean. Large correlation coefficient and small RMS indicate that the horizontal mean can represent the characteristic time evolution of horizontal homogeneous mixed-layer properties over model domain. Small correlation coefficient and large RMS indicate that the horizontal differences of mixed-layer properties over model domain are so large that there is no simply horizontal mean that can highlight the time evolution of mixed-layer properties for individual grid.

The correlation coefficients and RMS of mixed-layer temperature, salinity and depth for CB and CBT are shown in Fig. 9 and Fig. 10, respectively. The correlation coefficients of the mixed-layer temperature exceed 95 % confidence level (> 0.2), whereas those of the mixed-layer salinity (-0.9-0.9) includes some that do not exceed in CB (dark solid lines in Fig. 9). The RMS temperature differences are 0.2-0.4 $^{\circ}C$, and the RMS salinity differences are 0.2-0.5 PSU in CB (dark solid lines in Fig. 10). Since 1 PSU is 3.75 times larger than $1^{\circ}C$ in the density units, the correlations and RMS differences indicate a larger spatial fluctuations in mixed-layer salinity than temperature in CB.

To explain large spatial salinity fluctuations in CB, correlation and RMS of each term in mixed-layer thermal and salt budgets are examined. In general, the advection terms are small compared to entrainment and surface forcing. Thus, only correlation and RMS of entrainment and surface forcing are discussed in Fig. 11. First, the correlation coefficients of fresh water forcings (-0.1-0.4) are smaller than those of thermal forcings (0.6-0.9), whereas the RMS of fresh water forcings ($0-5 \text{ } PSU \text{ day}^{-1}$) is much larger than that of thermal forcings ($0-3 \text{ } ^{\circ}C \text{ day}^{-1}$) in terms of the density units. Second, the correlation coefficients of fresh water forcings are smaller than those of the saline entrainment (0-0.6) while the RMS of fresh water forcings is larger than that of the saline entrainment (0-2

$PSU\,day^{-1}$). Therefore, the fresh water forcing is responsible for larger spatial fluctuations in mixed-layer salinity in CB.

Why does the fresh water forcing have larger spatial fluctuations than the thermal forcing? With same distributions of mixed-layer depths, the different horizontal distributions between the fresh water forcing and the thermal forcing come from the different horizontal distributions between the fresh water flux and the heat flux. To understand the difference, the horizontal-mean versus the values along 366 km of the fresh water and heat fluxes are plotted in Fig. 13. This is a typical case where correlation coefficients of fresh water forcing and thermal forcing between horizontal mean and values at 366 km are 0 and 0.7 respectively. Most of the horizontal-mean fresh water fluxes are less than zero, which indicates that horizontal-mean precipitation occurs during most of integration period. Whereas most of fresh water flux at 366 km are around small positive values, which indicates that precipitation does not occur at this particular point during most of integration period. Fresh water flux at 366 km is so different from its horizontal-mean so that there is no correlation between them. Unlike the fresh water flux, the heat flux at 366 km and horizontal-mean heat flux are positive with dominance of solar flux during daytime, and negative with dominance of upward heat flux [the heat taken away from the ocean surface] which includes IR, sensible and latent heat fluxes during nighttime, though their magnitudes are different. Thus, large thermal correlation exists between horizontal mean and flux at 366 km.

To explain similar thermal variations in 1-D and 2-D ocean simulations without salinity effects, CAT and CBT in 22 December are analyzed. In the late morning - early afternoon of 22 December, the horizontal-mean mixed-layer depths are shallower in CBT (about 11 m) than in CAT (about 15 m) (Fig. 4c). Thus, the horizontal-mean heating rate is larger in CBT ($0.66^{\circ}C\,day^{-1}$) than in CAT ($0.25^{\circ}C\,day^{-1}$). In the late afternoon, the magnitudes of IR, sensible and latent heat fluxes start to be larger than those of solar flux, and the heat loss over ocean surface becomes dominant. Since the cooling rate is inversely proportional to the mixed-layer depth, shallower mixed layers with higher temperatures have larger cooling rates than do the deeper mixed layers with lower temperatures (not

shown), the horizontal-mean cooling rate in CBT ($-0.43^{\circ}\text{C day}^{-1}$) is larger than that in CAT ($-0.12^{\circ}\text{C day}^{-1}$). The mixed-layer temperatures in CBT become horizontally uniform. In the evening of 22 and early morning of 23 December, the mixed layers in CAT deepen to 50 m (Fig. 4c), and the horizontal-mean mixed-layer depths in CBT also become 50 m with their RMS of 2 m (Fig. 10c). This indicates that the mixed-layer depths in CBT are horizontally uniform, and are as deep as they are in CAT. Deep horizontally-uniform mixed layers cause weak horizontally-uniform cooling rates (The RMS is about 0 in Fig. 12). The horizontal-mean cooling rates in both experiments are about ($-0.1^{\circ}\text{C day}^{-1}$). Therefore, the RMS temperature differences in CBT become about 0 (Fig. 10a), and the mixed-layer temperature in both experiments are about the same.

To explore the cause of different thermal variations between 1-D and 2-D ocean simulations with salinity effects, CA and CB in 20-21 December are examined. In evening of 20 and early morning of 21 December, the thermal entrainment is weaker than the thermal forcing (Table 2b). The mixed-layer depths in CA are about 1-2 m (Fig. 4c). In CB, the horizontal-mean mixed-layer depths are about 5-13 m and the RMS depth differences are about 10-15 m (Fig. 10c). The large horizontal depth fluctuations result from shallow mixed layers over convective areas and deep mixed layers over convection-free areas (Fig. 8). The mixed-layers in CA are shallower than in CB so that the cooling rates in CA are larger than in CB. As a result, mixed-layer temperature becomes lower in CA than in CB.

The effect of fresh water flux on the ocean thermal balance can be summarized as follows. When the fresh water flux is not included, the surface heat flux and wind stress determine the mixed-layer depth. Although temperatures increase faster in shallower mixed layers than in deeper mixed layers due to solar heating in the late morning and early afternoon, they decrease faster in shallower mixed layers than in deeper mixed layers in the late afternoon when the heat loss becomes dominant. The nocturnal heat loss due to IR, sensible and latent heat fluxes deepens the mixed layers. Deep mixed layers cause small horizontally-uniform cooling rates. The horizontally-uniform temperatures are maintained. Thus, the mixed-layer depth controlled by surface heat flux in the thermal system plays a crucial role in regulating the nocturnal heat distribution in the upper ocean, and main-

taining similar temperature variabilities in the mixed layers in the coupled experiments with 1-D and 2-D ocean models. When the fresh water flux and salinity stratification are included in the model, the nocturnal deep mixed layer is not guaranteed. Instead, the precipitation will induce shallow mixed layers and large cooling rates during nighttime. The mixed-layer temperature variabilities in the coupled experiments with 1-D and 2-D ocean models becomes significantly different.

4. Summary

In this study, a coupled ocean-cloud resolving atmosphere model is used to investigate the impacts of convective scale ocean disturbances induced by atmospheric precipitation in the ocean mixed layer heat and salt budgets. The coupled model is mainly forced by the time-varying horizontally-uniform large-scale vertical velocity derived from TOGA COARE IOP during a seven-day period. Since the model is strongly controlled by the imposed forcing, the horizontal-mean surface momentum, heat, and fresh water fluxes simulated in the coupled model have similar magnitudes and variations to those simulated in the cloud resolving model with imposed observed SST. The comparison of 1-D simulation with observation at IMET buoy during TOGA COARE shows a reasonable agreement.

Surface forcing and entrainment are the dominate processes determining the mixed-layer variations. The thermal advection is not important. Salinity advection is equally important in the mixed-layer salinity budget during clear-sky condition, and negligibly small relative to surface forcing and entrainment during raining condition.

When the effects of fresh water flux and salinity are included in the coupled model, horizontal-mean mixed-layer temperature and salinity in 1-D ocean model experiment (CA) and 2-D ocean model experiment (CB) differ by about $0.4^{\circ}C$ and 0.3 PSU , respectively. The mean salinity difference is larger than the mean temperature difference in terms of their contributions to the mean density difference. In CB, the surface heat flux show significant diurnal signals with the dominance of downward solar radiation during daytime and dominance of upward flux (IR, sensible and latent heat fluxes) during nighttime at each

grid. As a result, there is strong thermal correlation among each grid. Since convective areas are usually surrounded by broad convection-free areas, horizontal-mean precipitation could occur, but the precipitation may not occur in most of the integration period, causing very low correlation between horizontal-mean and grid value of the fresh water fluxes. Since the rain rates vary significantly, the fresh water flux has much larger spatial fluctuations than the saline entrainment has. As a result, the fresh water flux determines large spatial salinity fluctuations, which contributes to large mean salinity difference between CB and CA.

When salinity effects are excluded, horizontal-mean mixed-layer temperatures in coupled experiments with 1-D (CAT) and 2-D (CBT) ocean model show similar variabilities. When salinity effects are included, the temperatures in coupled experiments with 1-D (CA) and 2-D (CB) ocean model display different variabilities. The mean nocturnal temperatures in CAT and CBT are about the same, and the maximum mean temperature difference between the two experiments ($0.15^{\circ}C$) is smaller than that between CA and CB ($0.4^{\circ}C$). When the fresh water flux is excluded in the model, the temperatures increase and then decrease faster in shallower mixed layers than in deeper mixed layers during daytime. The mixed-layer temperatures are horizontally uniform in the late afternoon. During nighttime, heat loss causes deep mixed layers and the cooling rates are weak and horizontally uniform so that the horizontally-uniform mixed-layer temperatures in 2-D ocean coupled experiment are maintained, and they are similar to temperatures in 1-D ocean coupled experiment. Therefore, the similar variabilities of mixed-layer temperatures can be simulated in 1-D and 2-D ocean coupled experiments when the effects of salinity and fresh water flux are not considered. However, the fresh water flux causes shallow mixed layers and large cooling rates in CA and over convective areas in CB while heat loss over ocean surface still induce deep mixed layers and small cooling rates over convection-free areas in CB during nighttime. The nocturnal temperatures show large horizontal fluctuations in CB, and their variabilities are different from those in CA.

This study demonstrates that deep mixed-layer during nighttime is a key for regulating mixed-layer temperature in the simulation without salinity. Thus, temperature simulation

of the OGCM without salinity could neglect the effect of convection-induced subgrid thermal disturbances. However, this study also demonstrates that the mixed-layer depth is so sensitive to precipitation that the horizontal fluctuations of salinity and temperature are enhanced in high-frequency variability. It should be point out again that since the convective time scale associated with the fresh water flux is about 1-2 hours, the mixing processes caused by the fresh water input are much more important than the other ocean processes.

The OGCM simulations have showed the important impacts of salinity and fresh water flux in the ocean temperature. The results in this study show that the impacts of salinity stratification associated with the atmospheric precipitation inputs on the ocean mixed-layer temperature could be biased, if the convective scale precipitation signals are filtered out. This nonlinear scale interactions between convective scale atmospheric precipitation (fresh water flux) and upper ocean salinity and temperature should be included in the OGCM by the proper parameterization scheme. It needs careful consideration in the parameterization design, and more sensitivity experiments by the OGCM.

Acknowledgments. This research is supported under the TRMM project of NASA's Mission to Planet Earth Office.

Table 1 Summary of five experiment designs

Exp	Model	Salinity
C1	2-D cloud model only	
CA	2-D cloud model and 1-D ocean model	Yes
CB	2-D cloud model and 2-D ocean model	Yes
CAT	2-D cloud model and 1-D ocean model	No
CBT	2-D cloud model and 2-D ocean model	No

Table 2 Horizontal and temporal means of zonal wind stress (Nm^{-2}), net surface heat flux (Wm^{-2}), and surface fresh water flux ($10^{-4} kgm^{-2}s^{-1}$) simulated in five experiments.

Exp	Wind stress	Heat flux	Water flux
C1	0.036	-39.6	1.70
CA	0.035	-34.6	1.74
CB	0.036	-33.0	1.69
CAT	0.036	-40.5	1.67
CBT	0.036	-40.9	1.78

Table 3 Horizontal and time-mean mixed-layer temperature change rates due to thermal entrainment (TE), surface thermal forcing (STF), temperature advection (TA), and their sum in CAT, CBT, CA, and CB. Unit is $^{\circ}C day^{-1}$.

(a) average within 8 p.m. of 20 -4 a.m. of 21 December

Experiment	TE	STF	TA	Sum
CAT	-0.09	-0.44	0.0	-0.53
CBT	-0.10	-0.46	-0.01	-0.57
CA	0.31	-2.38	0.0	-2.07
CB	0.20	-1.14	0.05	-0.89

(b) average within 2 p.m. - midnight of 22 December

Experiment	TE	STF	TA	Sum
CA	0.61	-0.54	0.00	0.07
CB	0.38	-0.92	0.12	-0.42

Table 4 Horizontal and time-mean mixed-layer salinity change rates within 1 a.m. - 11 a.m. of 22 December due to saline entrainment (SE), fresh water forcing (FWF), salinity advection (SA), and their sum in CA, CB. Unit is $PSU day^{-1}$.

Experiment	SE	FWF	SA	Sum
CA	0.33	-0.16	0.00	0.17
CB	0.17	-0.34	0.16	-0.01

References

- Adamec, D., R. L. Elsberry, R. W. Garwood, and R. L. Haney, 1981: An embedded mixed-layer-ocean circulation model, *Dyn. Atmos. Oceans*, **6(2)**, 69-96.
- Chou, M.-D., D. P. Kratz, and W. Ridgway, 1991: IR radiation parameterization in numerical climate studies. *J. Climate*, **4**, 424-437.
- Chou, M.-D., and M. J. Suarez, 1994: An efficient thermal infrared radiation parameterization for use in General Circulation Model. NASA Technical Memorandum 104606, Vol. 3, 85pp.
- Chou, M.-D., M. J. Suarez, C.-H. Ho, M. M.-H. Yan, and K.-T. Lee, 1997: Parameterizations for cloud overlapping and shortwave single-scattering properties for use in General Circulation and Cloud Ensemble Models. *J. Climate*, **11**, 202-214.
- Cooper, N.S., 1988: The effect of salinity on tropical ocean models, *J. Phys. Oceanogr.*, **18**, 697-707.
- Delcroix, T., L. Gourdeau, and C. Henin, 1998: Sea surface salinity changes along the Fiji-Japan shipping track during the 1996 La Nina and 1997 El Nino period. *Geophys. Res. Lett.*, (submitted).
- Gaspar, Ph., 1988: Modeling the seasonal cycle of the upper ocean. *J. Phys. Oceanogr.*, **18**, 161-180.
- Godfrey, J. S., and E. J. Lindstrom, 1989: The heat budget of the equatorial western Pacific surface mixed layer. *J. Geophys. Res.*, **94**, C6, 8007-8017.
- Krueger, S. K., Q. Fu, K. N. Liou and H.-N. S. Chin, 1995: Improvement of an ice-phase microphysics parameterization for use in numerical simulations of tropical convection. *J. Appl. Meteor.*, **34**, 281-287.
- Li, X., C.-H. Sui, D. Adamec, and K.-M. Lau, 1998: Impacts of precipitation in the upper ocean in the western Pacific warm pool during TOGA COARE. *J. Geophys. Res.*, **103**, C3, 5347-5359.
- Li, X., C.-H. Sui, K.-M. Lau, and M.-D. Chou, 1999: Large-scale gorging and cloud-radiation interaction in the tropical deep convective regime. *J. Atmos. Sci.*, **56**, 3028-3042.

- Lukas, R., and E. Lindstrom, 1991: The mixed layer of the western equatorial Pacific Ocean. *J. Geophys. Res.*, **96**, 3343-3457.
- McPhaden, M. J., 1993: TOGA-TAO and the 1991-1993 El Nino-Southern Oscillation Event. *Oceanography*, **6**, 36-44.
- McPhaden, M. J., 1995: The Tropical Atmosphere-Ocean Array is completed. *Bull. Am. Meteorol. Soc.*, **76**, 739-741.
- Miller, J.R., 1976: The salinity effect in a mixed-layer ocean model, *J. Phys. Oceanogr.*, **6**, 29-35.
- Murtugudde, R. and A. J. Busalacchi, 1998: Salinity effects in a tropical ocean model. *J. Geophys. Res.*, **103**, 3283-3300.
- Niiler, P. P., and E. B. Kraus, 1977: One-dimensional models, in *Modeling and Prediction of the Upper Layers of the Ocean*, edited by E. B. Kraus, Pergamon, New York, 143-172.
- Soong, S. T., and Y. Ogura, 1980: Response of tradewind cumuli to large-scale processes. *J. Atmos. Sci.*, **37**, 2035-2050.
- Soong, S. T., and W. K. Tao, 1980: Response of deep tropical cumulus clouds to mesoscale processes. *J. Atmos. Sci.*, **37**, 2016-2034.
- Sui, C.-H., K.-M. Lau, Y. Takayabu, and D. Short, 1997a: Diurnal variations in tropical oceanic cumulus ensemble during TOGA COARE. *J. Atmos. Sci.*, **54** 639-655.
- Sui, C.-H., X. Li, K.-M. Lau, and D. Adamec, 1997b: Multi-scale air-sea interactions during TOGA COARE. *Mon. Wea. Rev.*, **125**, 448-462.
- Sui, C.-H., X. Li, and K.-M. Lau, 1998a: Radiative-convective processes in simulated diurnal variations of tropical oceanic convection. *J. Atmos. Sci.*, **55**, 2345-2359.
- Sui, C.-H., X. Li, and K.-M. Lau, 1998b: Selective absorption of solar radiation and upper ocean temperature in the equatorial western Pacific. *J. Geophys. Res.*, **103**, C5, 10,313-10,321.
- Takayabu, Y. N., K.-M. Lau, and C.-H. Sui, 1996: Observation of a quasi-2-day wave during TOGA COARE. *Mon. Wea. Rev.*, **124**, 1892-1913.
- Tao, W.-K., and J. Simpson, 1993: The Goddard Cumulus Ensemble model. Part I: Model description. *Terr. Atmos. Oceanic Sci.*, **4**, 35-72.

- Vialard, J., and P. Delecluse, 1998a: An OGCM study for the TOGA decade. Part I: Role of salinity in the physics of the western Pacific fresh pool. *J. Phys. Oceanogr.*, **28**, 1071-1088.
- Vialard, J., and P. Delecluse, 1998b: An OGCM study for the TOGA decade. Part II: Barrier layer formation and variability. *J. Phys. Oceanogr.*, **28**, 1089-1106.
- Yang, S., K.-M. Lau, and P. S. Schopf, 1998: Sensitivity of the tropical Pacific Ocean to precipitation induced freshwater flux. *Climate Dynamics*, (submitted).
- You, Y., 1995: Salinity variability and its role in the barrier-layer formation during TOGA-COARE. *J. Phys. Oceanogr.*, **25**, 2778-2807.

Figure Captions

Fig. 1 Time evolution of (a) vertical velocity ($mb\ hour^{-1}$), and (b) zonal wind (ms^{-1}) taken from the TOGA COARE (Sui et al. 1997a) for a six-day period. Downward motion in (a) and westerly wind in (b) are shaded.

Fig. 2 Time evolution of (a) horizontal-mean zonal wind stress (Nm^{-2}), (b) net surface heat fluxes (Wm^{-2}), and (c) fresh water flux ($10^{-4}\ kg\ m^{-2}\ s^{-1}$) simulated in C1 (solid), and CA (dashed).

Fig. 3 Time evolution of (a) horizontal-mean mixed-layer temperature ($^{\circ}C$) and (b) 3-m salinity (PSU) simulated in CA (dashed). Solid lines denote observed SST in (a) and 3-m salinity in (b).

Fig. 4 Time evolution of (a) horizontal-mean mixed-layer temperature ($^{\circ}C$), (b) salinity (PSU), and depth (m) simulated in CAT (dotted), CBT (dark dashed), CA (light dashed), and CB (dark solid).

Fig. 5 Time evolution of (a) horizontal-mean thermal advection (dotted), thermal entrainment (dashed), thermal forcing (dark solid), and their sum (grey solid) and (b) horizontal-mean salinity advection (dotted), saline entrainment (dashed), fresh water forcing (dark solid), and their sum (grey solid) simulated in CB. Units of (a) and (b) are $^{\circ}C\ day^{-1}$ and $PSU\ day^{-1}$, respectively.

Fig. 6 (a) $\langle TF \rangle$ ($^{\circ}C\ m\ day^{-1}$) in CAT versus in CBT, (b) $\langle TF \rangle$ in CA versus in CB, (c) $\langle SF \rangle$ ($PSU\ m\ day^{-1}$) in CA versus in CB, (d) mixed-layer depth $\langle h_m \rangle$ (m) in CAT versus in CBT, and (e) $\langle h_m \rangle$ in CA versus in CB. See the definitions of TF and SF in (8a) and (8b) respectively.

Fig. 7 (a) surface thermal forcing STF versus STF1 ($^{\circ}C\ day^{-1}$) in CBT, (b) STF in CBT versus in CAT, (c) STF versus STF1 in CB, (d) STF in CB versus in CA, (e) surface fresh water forcing FWF versus FWF1 ($PSU\ day^{-1}$) in CB, and (f) FWF in CB versus in CA. See the definitions of STF, STF1, FWF, and FWF1 in (8c) and (8d), respectively.

Fig. 8 Time evolution of horizontal distributions of (a) surface precipitation (light shadings 0-10 $mm\ hour^{-1}$, dark shadings $> 10\ mm\ hour^{-1}$), (b) mixed-layer temperature ($28.75\ ^{\circ}C < \text{light shadings} < 29.25\ ^{\circ}C$, $29.25\ ^{\circ}C < \text{medium shadings} < 29.75\ ^{\circ}C$, dark shadings

> 29.75 °C), (c) mixed-layer salinity (33.75 PSU < light shadings < 34.0 PSU, 34.0 PSU < medium shadings < 34.25 PSU, dark shadings > 34.25 PSU), and (d) mixed-layer depth (2 m < light shadings < 10 m, 10 m < medium shadings < 20 m, dark shadings > 20 m) simulated in CB.

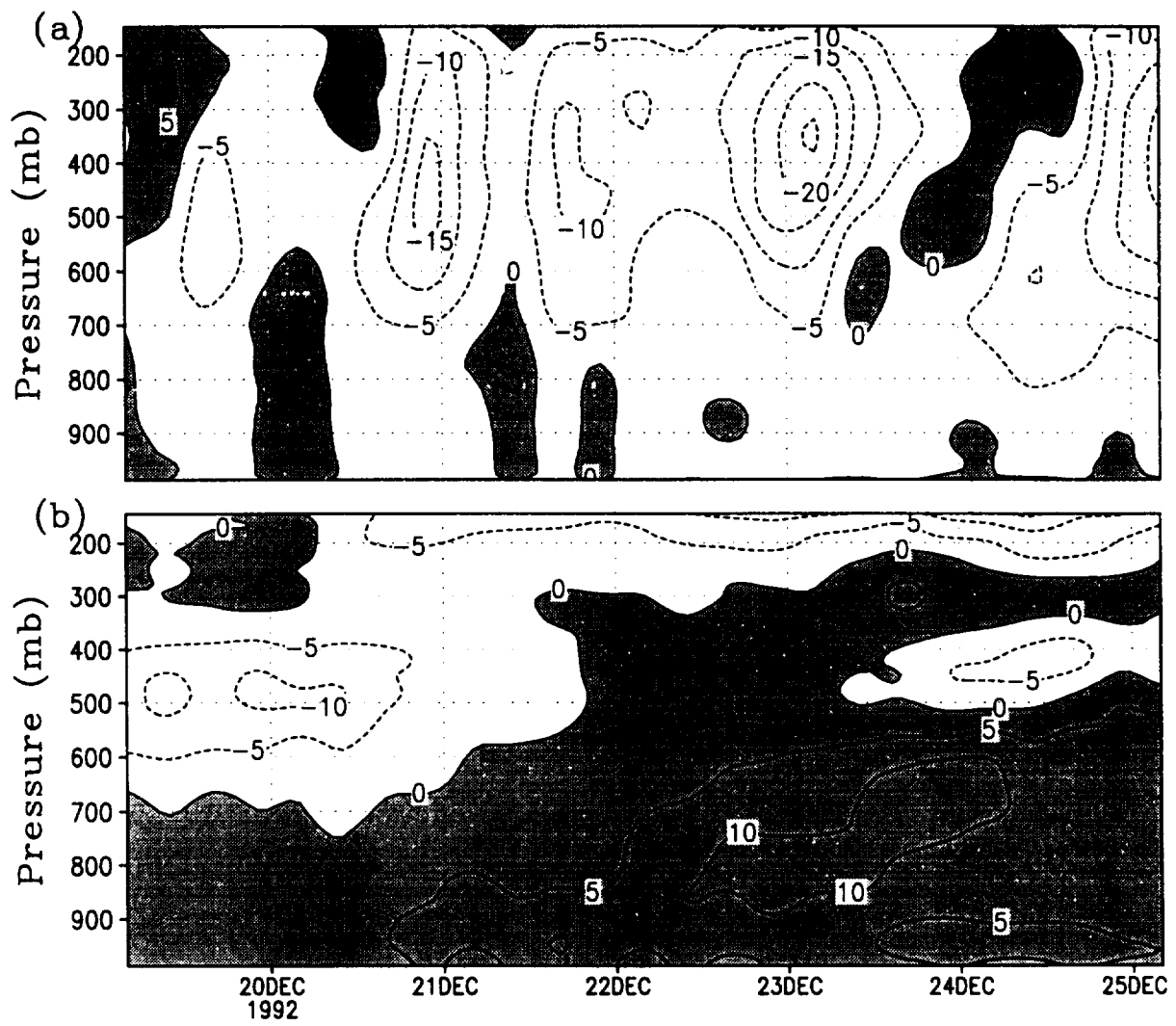
Fig. 9 Horizontal distributions of correlation coefficients (R) for (a) mixed-layer temperature, (b) salinity, and (c) depth simulated in CB (dark solid), and CBT (dashed), respectively. The correlation coefficient curves above upper dotted line or below lower dotted line exceed 95 % confidence level. See the definition of R in (9a).

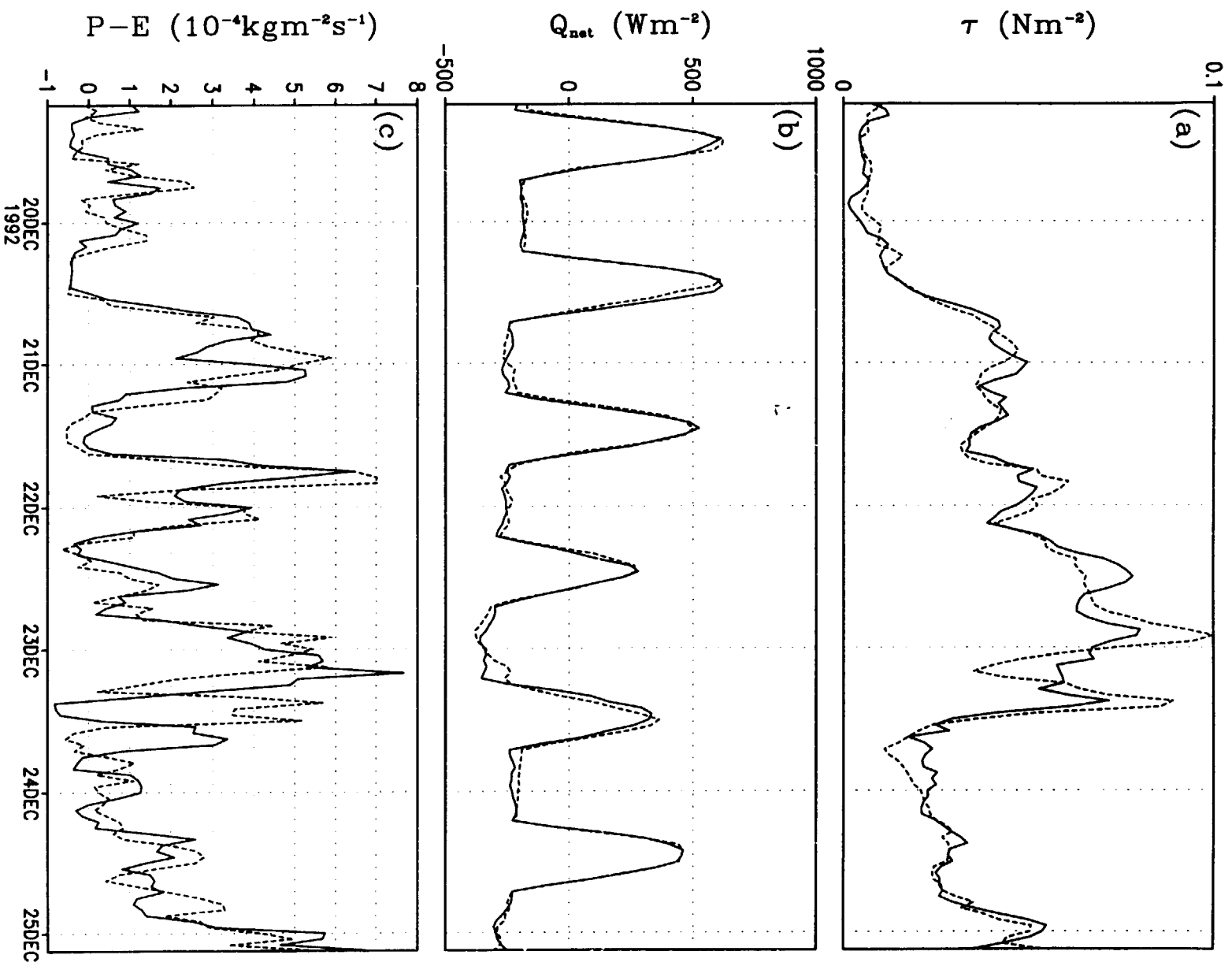
Fig. 10 Time evolution of RMS (D) for (a) mixed-layer temperature (°C), (b) salinity (PSU), and (c) depth (m) simulated in CB (dark solid), and CBT (dashed), respectively. See the definition of D in (9b).

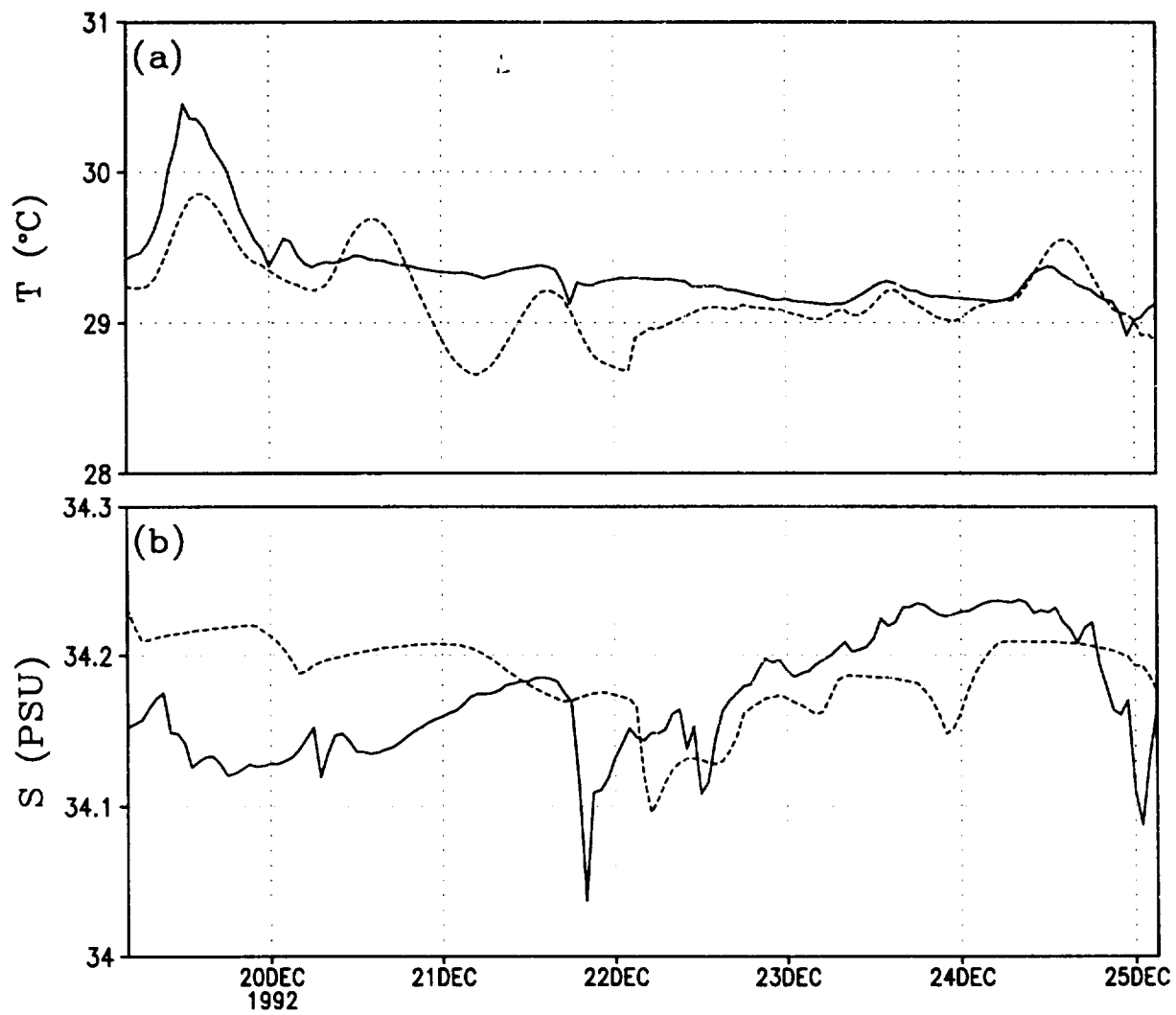
Fig. 11 Horizontal distributions of correlation coefficients (R) for (a) thermal entrainment (TE), (b) surface thermal forcing (STF), (c) saline entrainment (SE), and (d) fresh water forcing (FWF) simulated in CB (dark solid), and CBT (dashed), respectively. The correlation coefficient curves above upper dotted line or below lower dotted line exceed 95 % confidence level. See the definition of R in (9a).

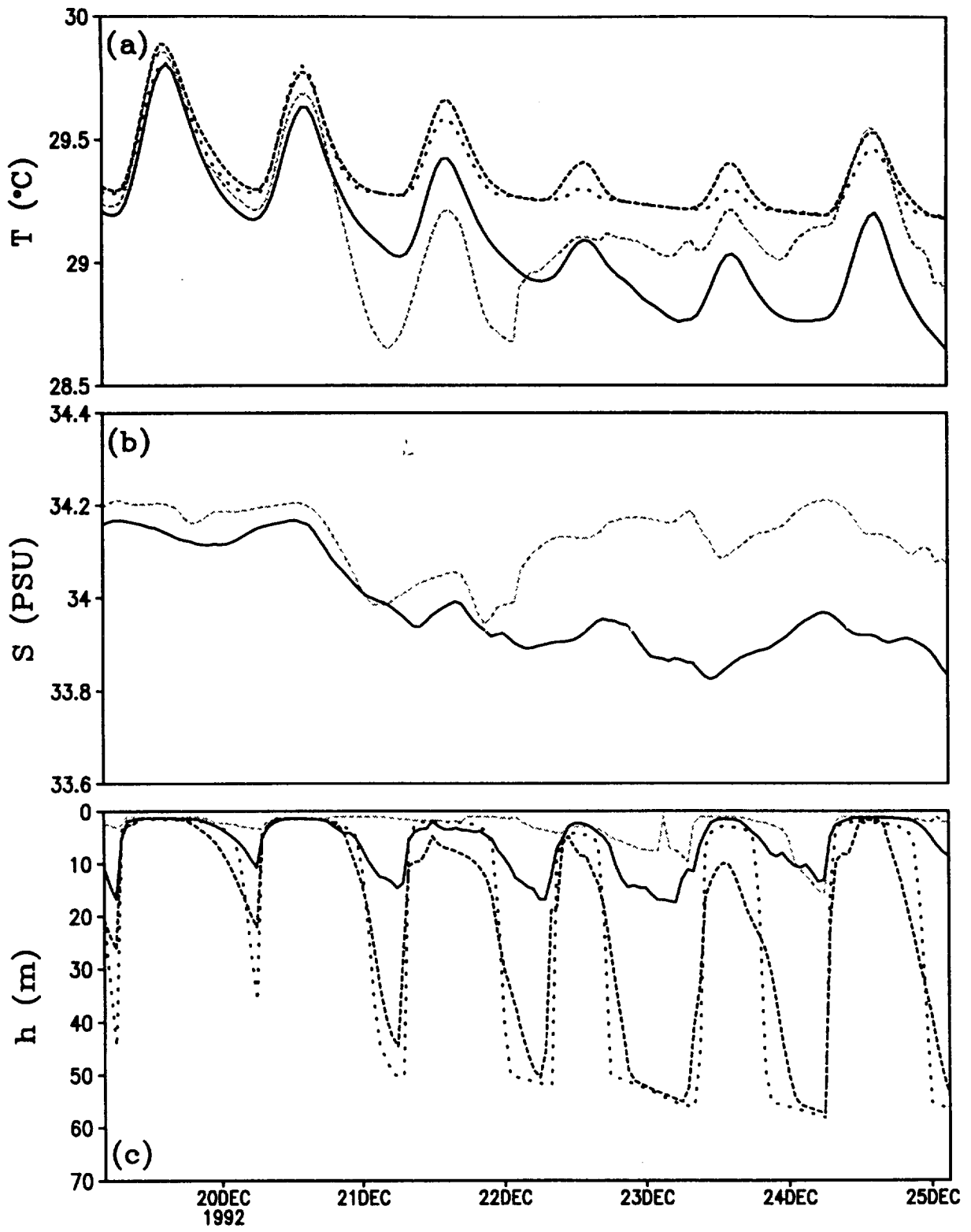
Fig. 12 Time evolution of RMS (D) for (a) thermal entrainment (TE), (b) surface thermal forcing (STF) ($^{\circ}C day^{-1}$), (c) saline entrainment (SE), and (d) fresh water forcing (FWF) ($PSU day^{-1}$) simulated in CB (dark solid), and CBT (dashed), respectively. See the definition of D in (9b).

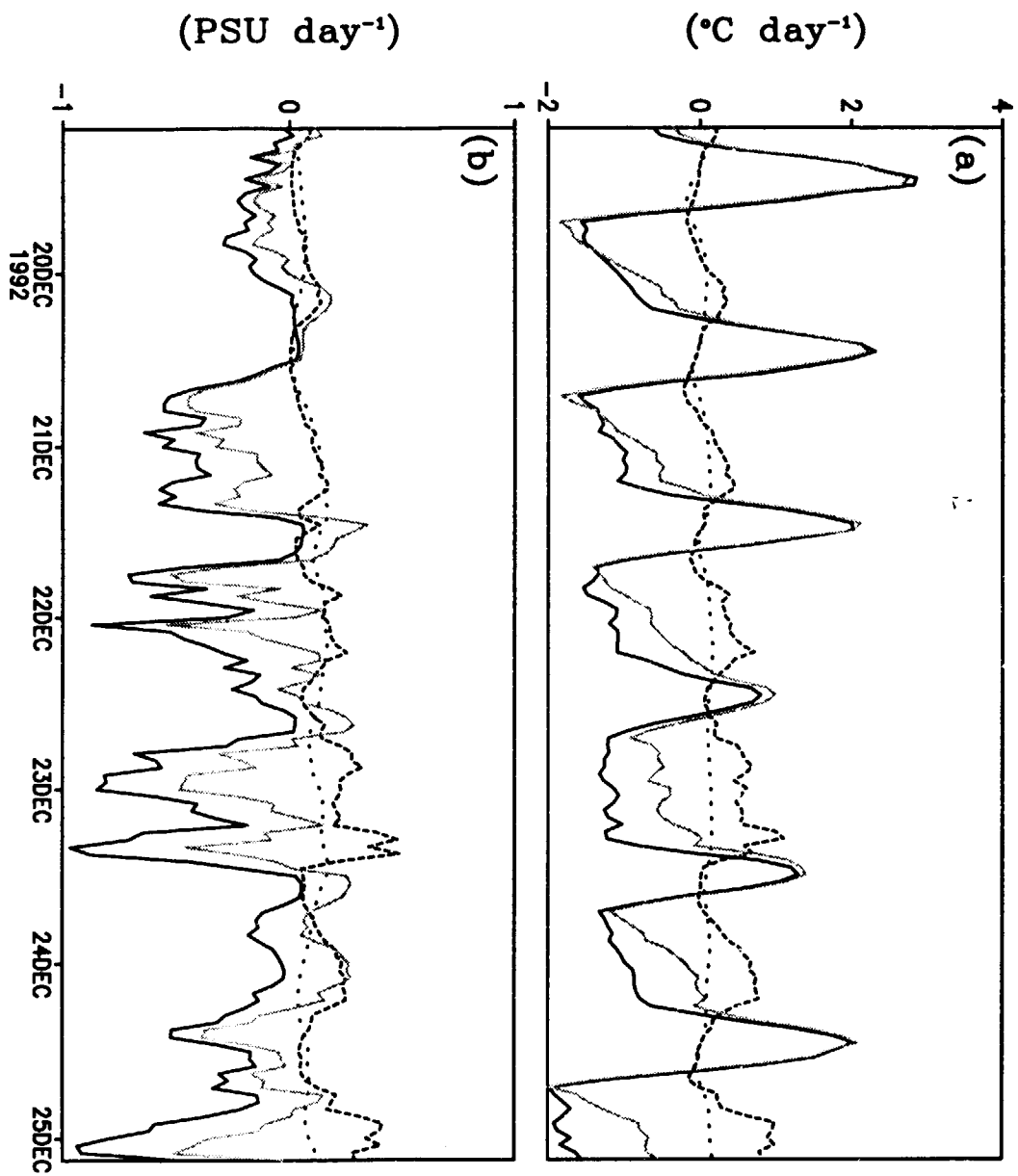
Fig. 13 Horizontal mean versus the grid values at 366 km of hourly surface fresh water flux $[-S_m(P - E)]$ (closed dots) and heat flux $[Q_o + I(0) - I(h_m)]$ (open dots) absorbed in the mixed layer in CB. Units of surface fresh water and heat fluxes are $0.01 PSU kg m^{-2} s^{-1}$ and $43 W m^{-2}$, respectively.

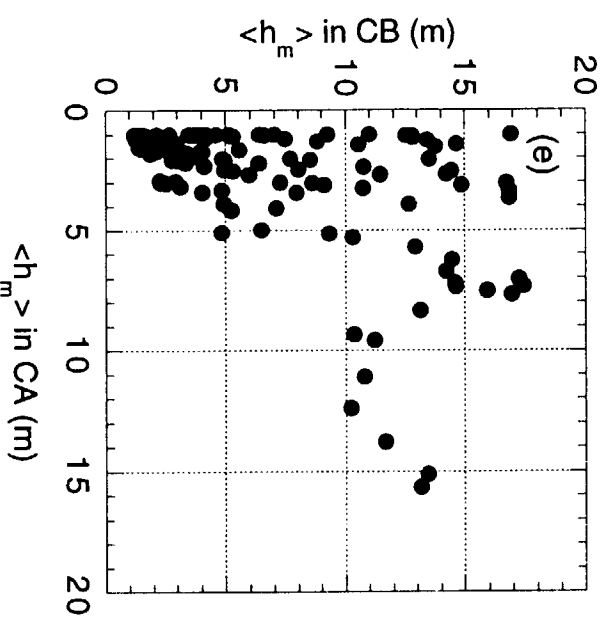
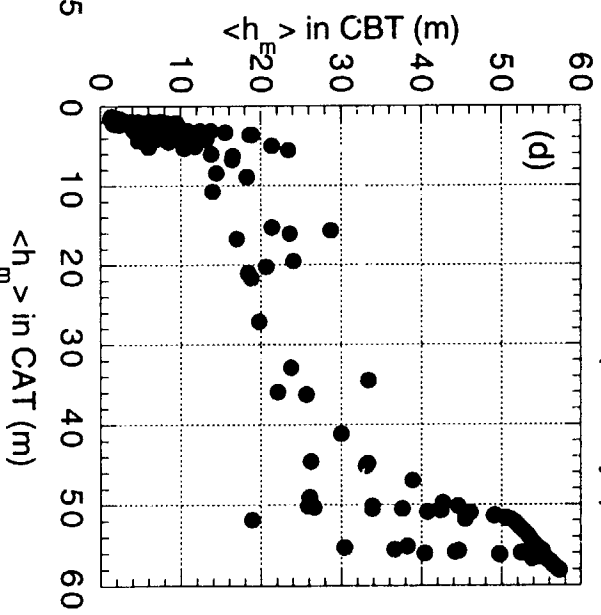
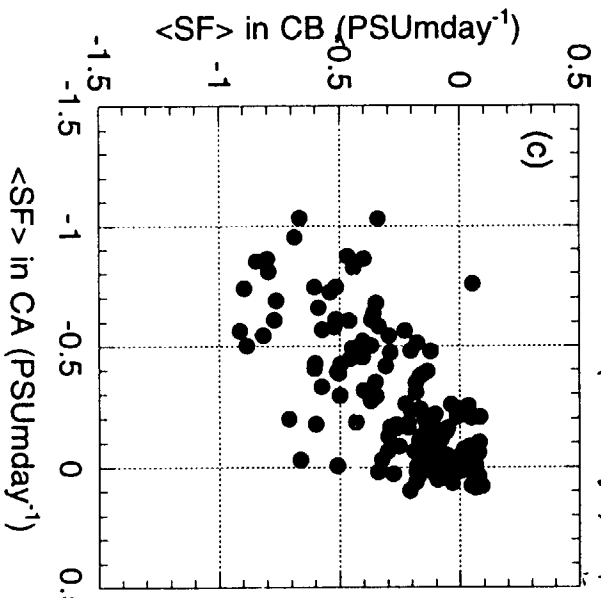
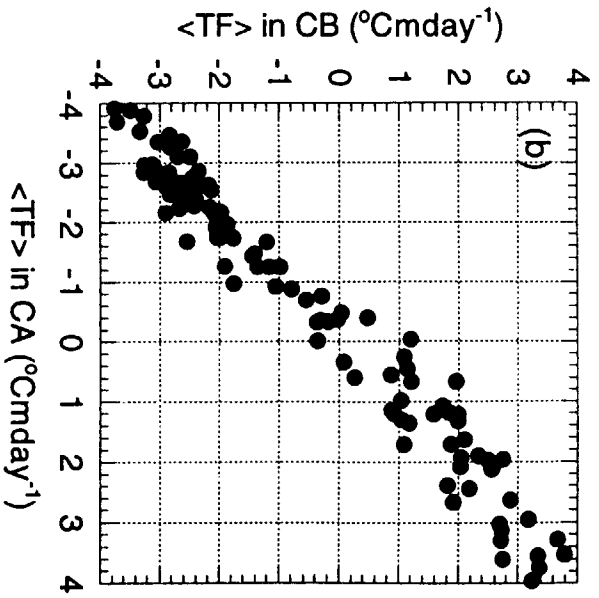
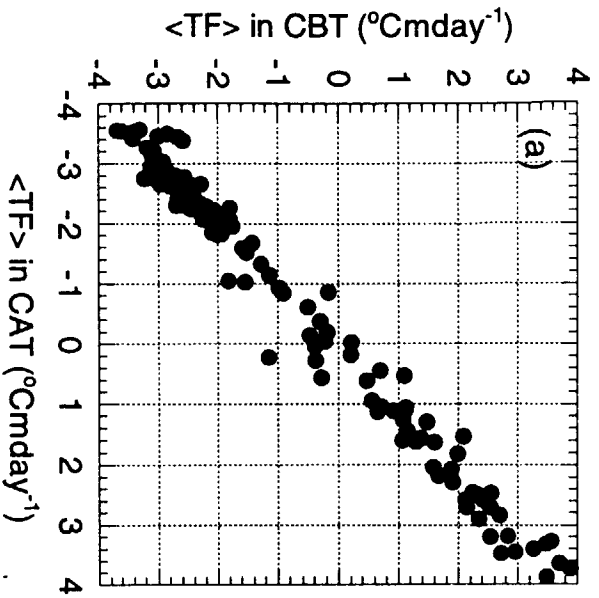


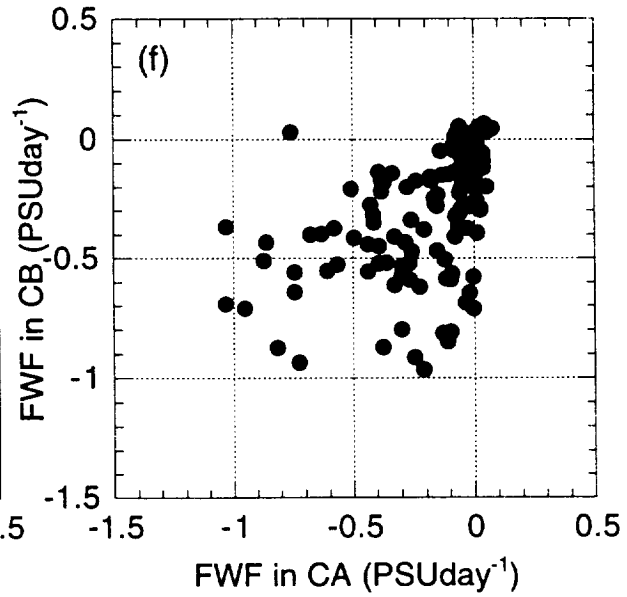
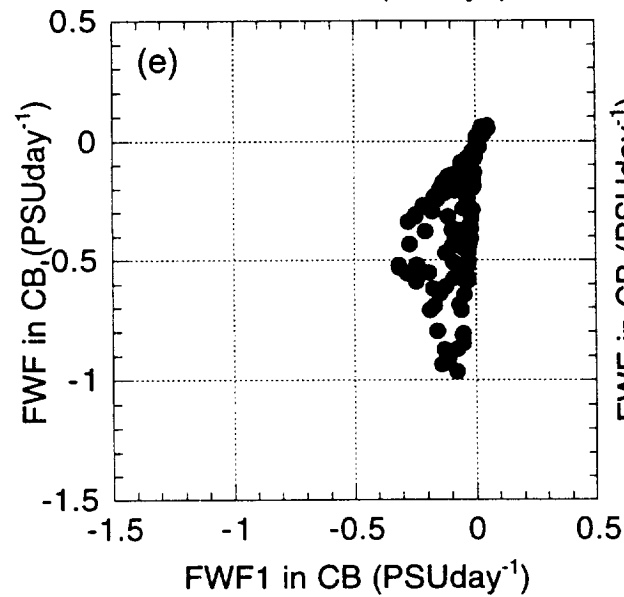
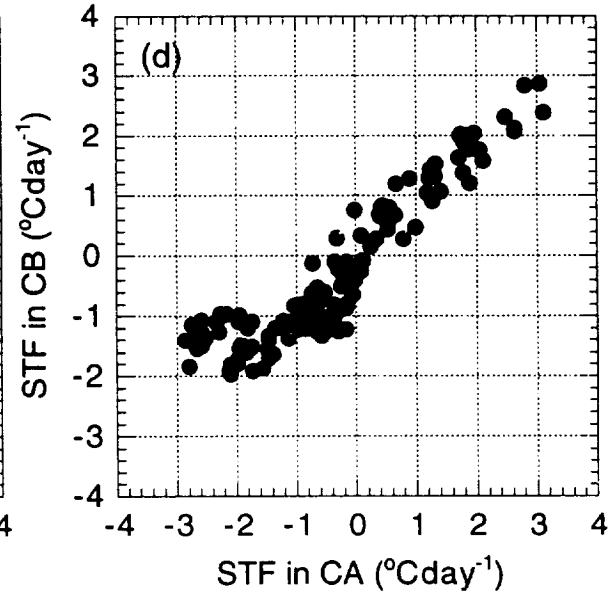
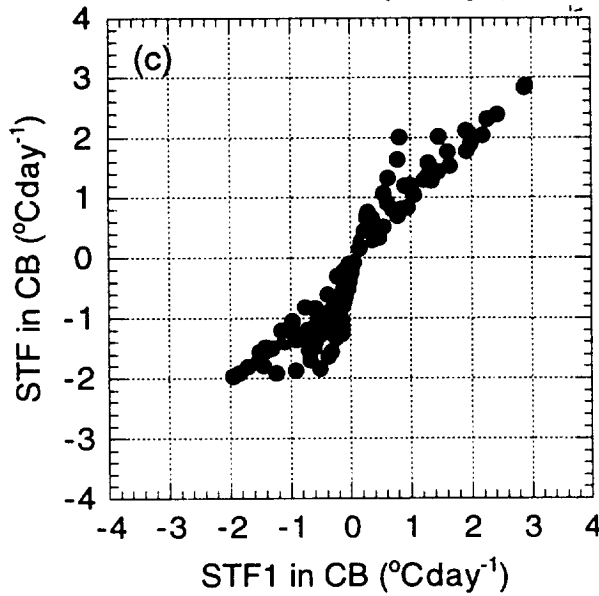
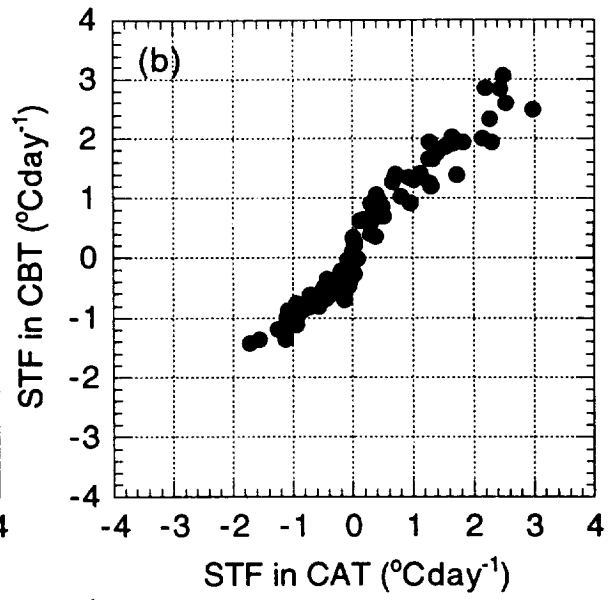
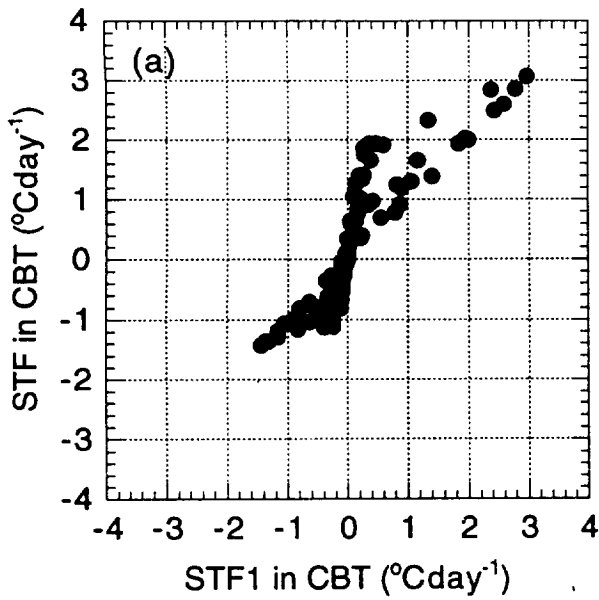


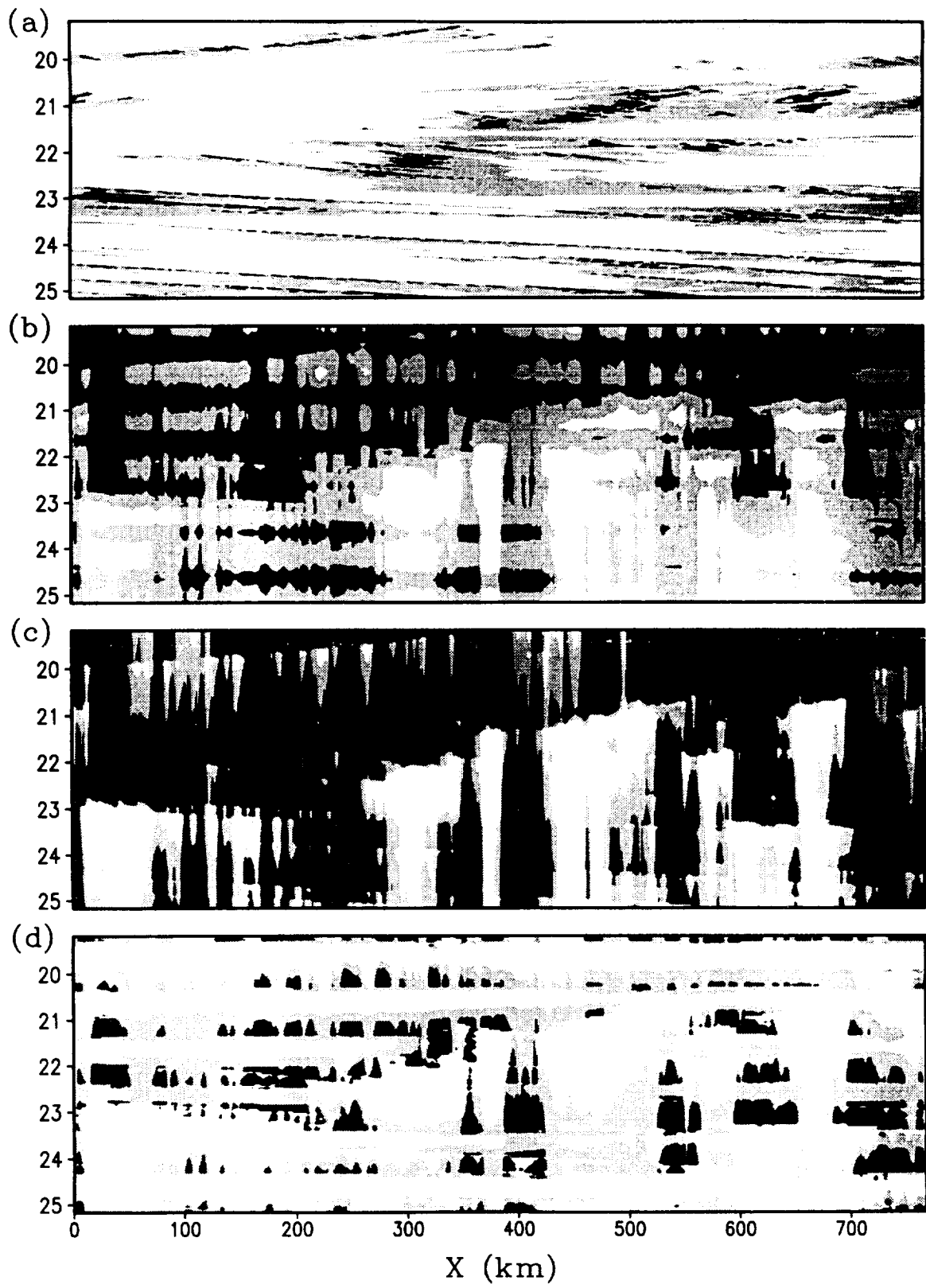


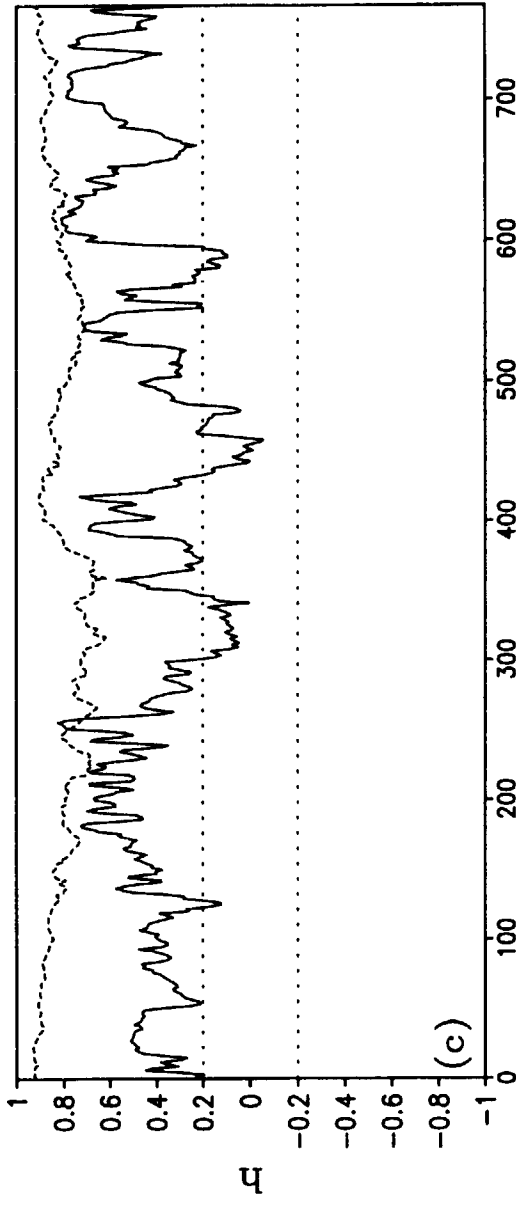
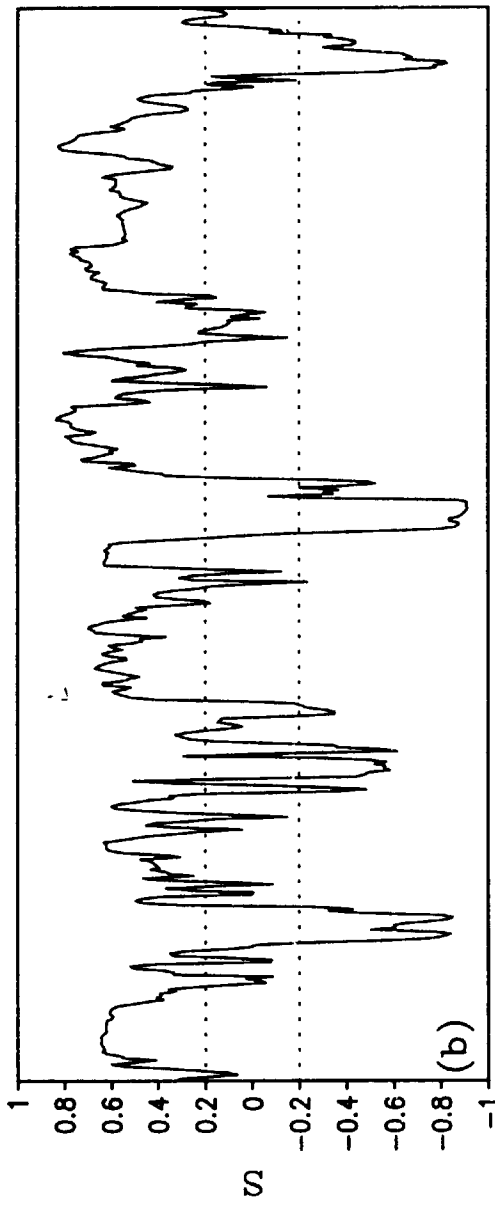
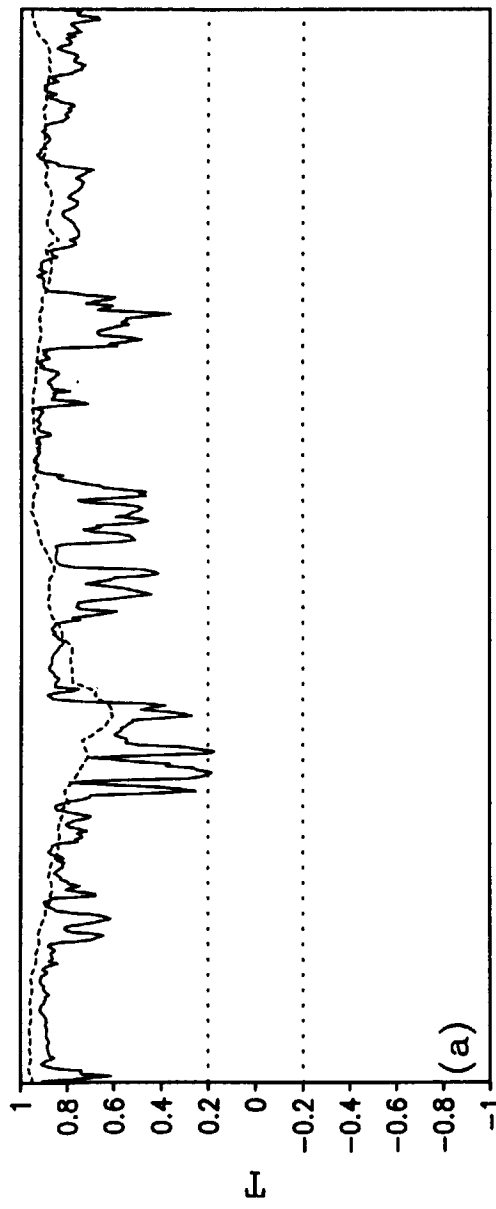












X (km)

